LETTER
SPACE PHYSICS

Earth and Planetary Physics
9: 995–1000, 2025
doi: 10.26464/epp2025025

A direct evidence for kilometric continuum generation through mode conversion

ZhouKun Deng[1,2], FuLiang Xiao[1,2*], QingHua Zhou[1,2*], YiHua He[1], Sai Zhang[1,2], Si Liu[1,2], JiaWen Tang[1,2], and Ping Li[1,2]

[1]School of Physics and Electronic Sciences, Changsha University of Science and Technology, Changsha 410114, China;

[2]Hunan Province Higher Education Key Laboratory of Modeling and Monitoring on the Near-Earth Electromagnetic Environments, Changsha University of Science and Technology, Changsha 410114, China

Key Points:

- Simultaneous observations of electrostatic waves, Z-mode, and kilometric continuum are reported.
- The radio window for mode conversion is derived from the fully-thermal dispersion relation.
- Simulations demonstrate that the electrostatic mode can convert to Z-mode, and then to the kilometric continuum at the radio window.

Citation: Deng, Z. K., Xiao, F. L., Zhou, Q. H., He, Y. H., Zhang, S., Liu, S., Tang, J. W., and Li, P. (2025). A direct evidence for kilometric continuum generation through mode conversion. *Earth Planet. Phys.*, *9*(4), 995–1000. http://doi.org/10.26464/epp2025025

Abstract: The origin of the Kilometric Continuum (KC) is usually attributed to the linear mode conversion window theory, yet direct evidence has been lacking. Here we present an event where electrostatic waves, Z-mode, and KC were observed simultaneously near the magnetic equator by the Van Allen Probes. We identify the radio window (the region for mode conversion taking place) at L = 4.059 by solving the fully-thermal dispersion relation. Ray tracing simulations show that the backward-propagating electrostatic mode can smoothly transition to Z-mode. Then, Z-mode can convert to KC when its direction shifts to parallel or anti-parallel propagation at the radio window, which aligns with observations. This study provides direct evidence that supports the linear mode conversion theory as an effective mechanism for KC generation.

Keywords: kilometric continuum; ray trace; linear mode conversion

Plain Language Summary

The Kilometric Continuum (KC) is a high-frequency electromagnetic wave commonly found near the Earth's equator. Theoretically, KC is believed to be produced by electrostatic waves near the upper hybrid frequency through a process called linear mode conversion, which tends to occur in areas with rapidly decreasing plasma density. However, finding the solid evidence for this has been challenging. In this study, we report an event where electrostatic waves, Z-mode, and KC were all seen together near the equator by the Van Allen Probes. We defined the "radio window" at L = 4.509, the area where mode conversion happens, by solving the fully-thermal dispersion relation, which describes how waves behave in a plasma. Our simulations showed that the backward-propagating electrostatic waves can easily change into Z-mode. After this, Z-mode can switch to KC when its direction shifts to parallel or anti-parallel propagation. This research provides the direct evidence that supports the idea that the linear mode conversion is an important process in generating KC.

First author: Z. K. Deng, ZhouK_Deng@foxmail.com
Correspondence to: F. L. Xiao, flxiao@126.com
Q. H. Zhou, tedchow@163.com

Received 28 NOV 2024; Accepted 14 FEB 2025.
First Published online 05 MAR 2025.

1. Introduction

The Kilometric Continuum (KC) is a form of high-frequency Non-thermal Continuum radiation (NTC) that was first detected by the Geotail satellite (Green and Boardsen, 2006; Hashimoto et al., 2006). The KC appears as a continuum of emissions in multi-narrow bands, which lasts for several hours (Hashimoto et al., 2005, 2006). The term "kilometric" refers to the wavelengths of the radiation, which can be on the order of kilometers. Similar to the other well-known kilometric radio emission, Auroral Kilometric Radiation (AKR), the KC typically exhibits frequencies above the upper hybrid frequency (f_{uh}) and partially overlaps with AKR in the frequency range (Hashimoto et al., 1999, 2006). Similar kilometric radiations have been observed on other magnetized planets. Gurnett et al. (1996) have reported observations of kilometric radio emissions on Jupiter by Galileo.

In comparison to AKR, KC's power spectral density (PSD) is significantly lower, often several orders of magnitude weaker. This makes it difficult to distinguish KC from AKR when AKR is particularly intense (Menietti et al., 2005; Zhang S et al., 2021; Li P et al.,

2024). Additionally, the source regions of KC and AKR are different. AKR is generated in the low-density polar cavity of Earth (Benson, 1975; Xiao FL et al., 2007, 2016, 2022; Zhang S et al., 2024), while KC is believed to originate from the plasmapause within equatorial structures known as notches or shoulders (Morgan and Gurnett, 1991; Green, 2004). Ray tracing simulations have identified the generation of KC at depths within the plasmasphere, and correlations between KC observations and plasmaspheric notches have been established through Geotail observations and IMAGE EUV images (Green, 2002). KC has also been observed to be beamed into emission cones with low latitudes ($\pm 15^{\circ}$) (Hashimoto et al., 2005, 2006).

Previous works have demonstrated that KC exists as the left-hand ordinary (LO) mode (Green and Boardsen, 2006; Hashimoto et al., 2006). The Linear Mode Conversion "Window" Theory (LMCWT) offers a theoretical framework for the generation of KC (Jones, 1976, 1981). According to LMCWT, electrostatic waves, which are close in frequency to f_{uh}, are the primary energy source for KC. These waves can refract in a density gradient perpendicular to the magnetic field, transforming into the electromagnetic Z-mode. As the Z-mode propagates to the radio window, where its frequency equals the plasma frequency (f_{pe}), its energy is transferred to the LO mode (Budden, 1980; Horne, 1989). The radio window is here defined as the intersection of the dispersion curves of the Z and LO mode by following Horne (1989). Observations of electrostatic waves and the Z-mode on Jupiter by the Juno spacecraft, as well as by the Cassini spacecraft (Menietti et al., 2018; Long MY et al., 2021), suggest that mode conversion processes may also occur on other magnetized planets. However, due to the limited data, there is still in lack of direct observational evidences for such mode conversion process, which remains a significant objective for this study.

2. Correlated Observation

The Van Allen Probes, positioned primarily at low latitudes (λ = ±20°), operate within an orbital range that allows them to frequently observe the plasmapause. Their perigee and apogee are approximately 675 kilometers and 31,250 kilometers above the Earth's surface, respectively. These probes are equipped with the Electric and Magnetic Field Instrument Suite and Integrated Science (EMFISIS) wave detectors, which include a High-Frequency Receiver module capable of detecting electric fields in the 10–500 kHz frequency range (Kletzing et al., 2013). Additionally, the Helium, Oxygen, Proton, and Electron Mass Spectrometer from the Energetic Particle, Composition, and Thermal Plasma Suite on board the Van Allen Probes can measure the density of energetic electrons necessary for related calculations (Spence et al., 2013).

Drawing from previous research (Kalaee and Katoh, 2016), a mode conversion case for Kilometric Continuum (KC) can be identified in a spectrogram by the following characteristics: (1) a harmonic structure of an electron electrostatic mode, (2) an enhanced upper hybrid wave, (3) KC near the upper hybrid frequency, and (4) a sharp plasma density gradient. An examination of wave data from the Van Allen Probes within the 30–500 kHz range revealed a distinct case where KC exhibited these linear mode conversion features, as illustrated in Figure 1.

Figure 1a shows the SYM-*H* and *AE* indices on November 16, 2015. The SYM-*H* index fell to nearly −40 nT, indicating a weak geomagnetic storm, while the *AE* index reached approximately 200 nT, corresponding to a weak substorm. Figure 1b depicts the variation in the cold electron density, with the gray area highlighting the period from 01:32 to 01:45 UT, during which enhanced KC was detected by Probe B. At this time, Probe B was situated at the magnetic latitude (Mlat) of approximately ~0.4° and the magnetic local time (MLT) of 10.7–11.0. The cold electron density changes are indicated in the gray area of Figure 1b. Theoretical studies suggest that a significant decrease in cold plasma density can facilitate the process of wave mode conversion.

In Figure 1c, the differential fluxes of energetic electrons (1–10 keV) increased by an order of magnitude, potentially providing the free energy needed for the generation of electrostatic waves. Figure 1d shows the detection of several harmonic structures of electrostatic waves with frequencies around 50–100 kHz. An enhanced Z-mode wave near the upper hybrid frequency (~95 kHz) with a power spectral density (PSD) of approximately ~10^{-6} $mV^2/m^2/Hz$ was also observed during this period. KC was observed at higher frequencies (~90–400 kHz) with the PSD ~10^{-8} $mV^2/m^2/Hz$. The intense waves near the upper hybrid frequency (plotted as the black line) and narrow-band waves are observed in the same frequency. These correlated observations suggest that the mode conversion likely occurred among KC, the electrostatic wave, and the Z-mode. KC at higher frequencies may be generated by mode conversion at other location and propagates here.

3. Numerical Simulation

In this study, we utilize a computational program developed based on the methodology of the HOTRAY code to simulate the mode conversion process of electromagnetic waves in the Earth's magnetosphere (Horne, 1989). The Earth-centered coordinate system and the local coordinate system are employed, consistent with previous ray-tracing works (Xiao FL et al., 2007, 2016; Guo MY et al., 2020; Deng ZK et al., 2022). Key factors influencing the generation and propagation of these waves include the magnetic field and background electron density (Guan CY et al., 2020; Fan K et al., 2021; Zhou QH et al., 2022; Li T et al., 2023). We adopt the global core plasma density model for the background electron density and represent the background magnetic field using a dipole field model (Gallagher et al., 2000). The hot plasma distribution is modeled using the approach proposed by Engel and Kennel (1985).

Figure 2 displays the dispersion curves corresponding to the observation at 1:37 UT in Figure 1c. The wave number k is normalized to the electron gyroradius (ρ) of 7.754 m. The dashed and solid lines represent the wave modes at normal angles of 0° and 90°, respectively. The resonance frequency f_q of the electrostatic mode, which corresponds to the point $\partial\omega/\partial k = 0$ on the dispersion curve, is identified. The electrostatic mode would be reflected when the wave frequency approaches the local f_q. As the electrostatic mode (θ = 90°) propagates backward, the normalized

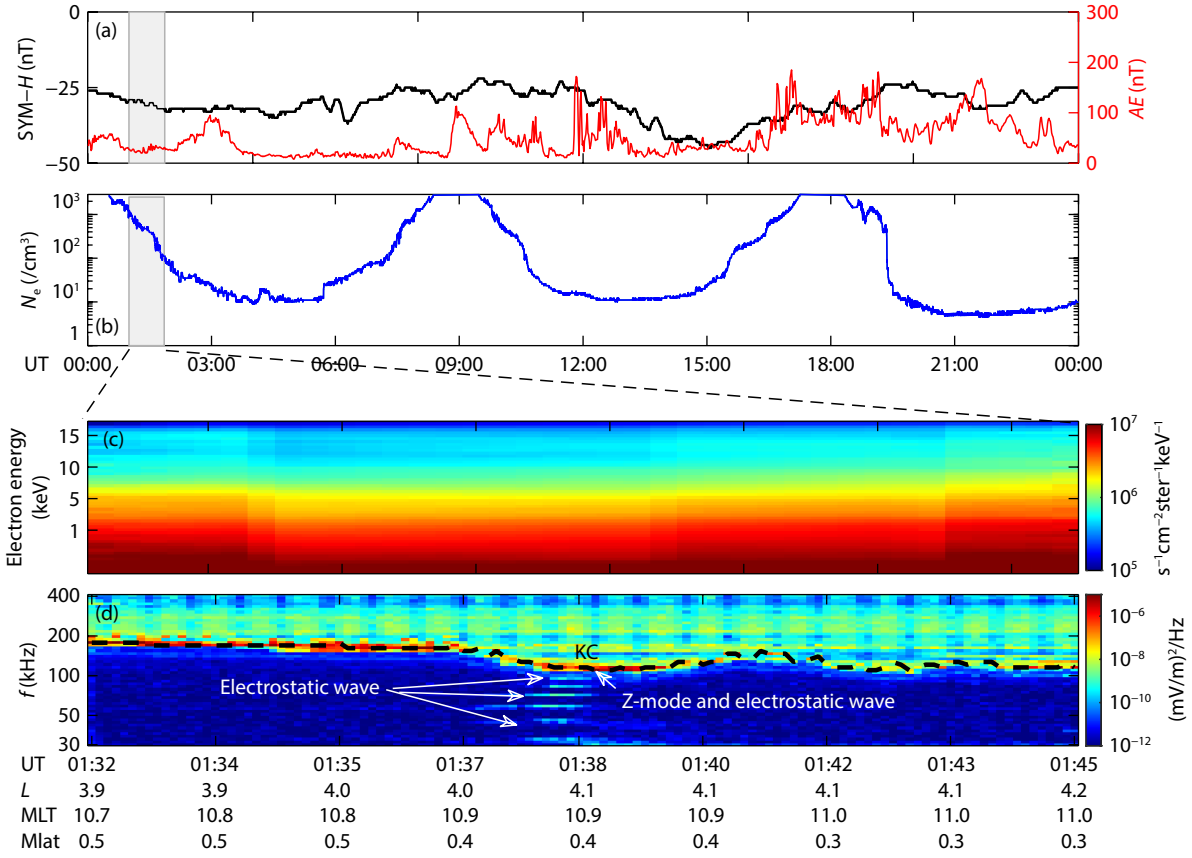

Figure 1. (a) The SYM-*H* index (black line) and *AE* index (red line) during 16 November 2015. (b) The electron density variation. Time periods marked by gray area correspond to (c) the variation of the differential flux of warm electrons and (d) the simultaneous observation of LO, Z, and electrostatic modes from Probe B.

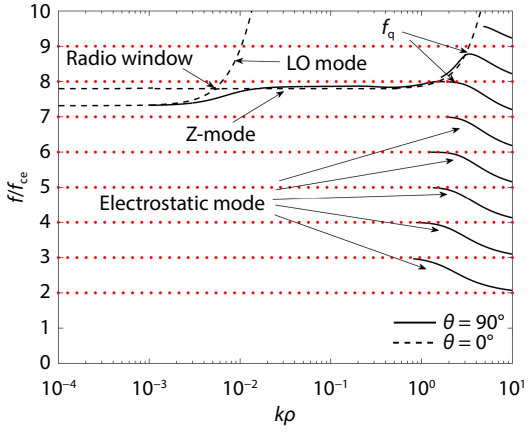

Figure 2. The dispersion curves of LO, Z, and electrostatic modes near the equator. The curves are calculated by using the initial wave normal angles $\theta = 90°$ (black solid lines) and $\theta = 0°$ (black dashed lines), respectively. The wave number k is normalized to the electron gyroradius ρ. Red dot line represents nf_{ce}.

frequency and wave number decrease, leading to a smooth connection of the dispersion curve ($\theta = 90°$) to the Z-mode ($\theta = 90°$). This connection of dispersion curves provides a pathway for the mode convection from the electrostatic mode to the Z-mode in the perpendicular direction. Moreover, the dispersion curve for the Z-mode intersects with that of the LO mode in the parallel direction ($\theta = 0°$). If the wave normal angle of the perpendicular-propagating Z-mode, transitioned from the electrostatic mode, decreases to $\theta = 0°$ during propagation, it can further convert into the LO mode (KC). Z-mode propagates between the lower frequency cutoff $f_z = 0.5\sqrt{f_{ce}^2 + 4f_{pe}^2} - f_{ce}$ and the upper hybrid frequency $f_{uh} = \sqrt{f_{ce}^2 + f_{pe}^2}$. Figure 2 shows that the parameter regime of $f_{pe}/f_{ce} > 7$, both f_z and f_{uh} are close to the f_{pe}. Therefore, the Z-mode exists near the f_{uh}. The intensity of Z-mode waves is larger than that of electrostatic waves probably because partial energy of electrostatic waves has already been transferred to Z-mode waves. In addition, Z-mode may be generated by another mechanism, which will be left for the future study.

A complete liner mode conversion process shows the electrostatic wave can change into Z-mode near the upper hybrid frequency. Z-mode will switch to LO mode where the wave frequency equals the plasma frequency. Thus, the spatial location of the radio window can be determined by the intersection of the three frequency curves. Our case was observed by Probe B at the equator. According to the theoretical prediction, the free space radiation emerging from the radio window will form two symmetrical beams about the magnetic equator (Boardsen et al., 2008). It is reasonable for the source region of the simulation to be set in the equatorial region. For this event, the location of the radio window is estimated as shown in Figure 3. The black solid lines represent nf_{ce} calculated using the dipole field. The blue line denotes the

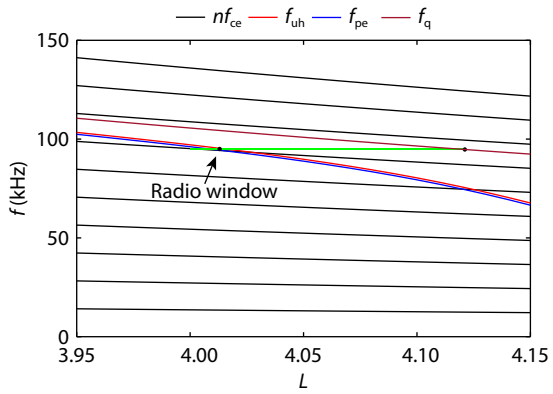

Figure 3. Several characteristic frequencies of the plasma that vary with R_E. The green line shows the region where the electrostatic mode (~95 kHz) can propagate.

local plasma frequency f_{pe}, calculated by employing the plasma density model mentioned above. The upper hybrid frequency f_{uh} is plotted by an orange line. The red line represents the resonance frequency f_q. Since the frequency of the electrostatic mode (~95 kHz) is confined within nf_{ce} and f_q, the electrostatic mode would exist in the region L = 4.012−4.121, as represented by the green line. Because the Z-mode should lie between f_{pe} and f_{uh}, the section of the green line between f_{pe} and f_{uh} (L = 4.059) is the location where the mode conversion can take place, known as radio window, as denoted by the black dot in Figure 3.

The mode conversion process simulated by the ray-tracing model is shown in Figure 4. The ray paths indicate that the electrostatic mode originating at L = 4.033, Mlat = 0.44° and Mlat = −0.44° propagates outward. The electrostatic mode is reflected at L = 4.121 where $f = f_q$. As the dispersion curve shows, the group velocity of the waves reverses at this point, indicating that these waves turn to inward propagation. When the electrostatic mode propagates to a position near the radio window L = 4.067 (hollow circle), where the frequency of the electrostatic mode equals f_{pe}, it may transform into the Z-mode. Figure 4b shows the variation of the wave normal angle near the window for both the Z-mode and the electrostatic mode. Both modes propagate almost perpendicular to the ambient magnetic field before the electrostatic mode reaches L = 4.12($f = f_q$). As the electrostatic mode propagates backward to L = 4.067, it converts into Z-mode. The wave normal angle of the Z-mode tends to become smaller during the subsequent propagation and is reflected due to the sharp plasma density gradient at L = 4.052. Subsequently, the parallel (anti-parallel) propagating Z-mode converts into the LO mode (KC) at the radio window L = 4.059, as predicted by the LMCWT.

4. Conclusion

An interesting event was observed where electrostatic waves, Z-mode, and KC were simultaneously present near the Earth's equator within L = 4.014−4.125, at MLT = 10.9 and Mlat = 0.4°, during the relatively quiet period on November 16, 2015. The following conclusions are drawn from the observations by the Van Allen Probes and the ray tracing simulation results, which support the linear mode conversion theory as a mechanism for KC generation:

(1) The radio window for the mode conversion is derived by solving the fully-thermal dispersion equation at the condition where the wave frequency equals the plasma frequency ($f = f_{pe}$). We identify the radio window location by calculating the intersection of three

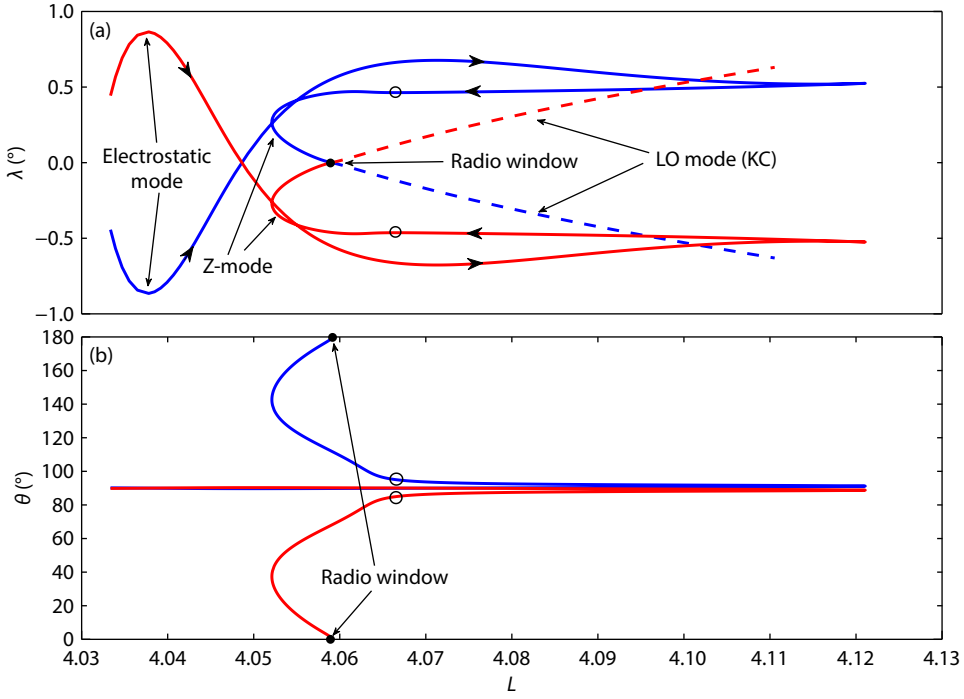

Figure 4. (a) Simulation results of LO, Z and electrostatic modes with the frequency ~95 kHz. (b) The variation of the wave normal angle during the propagation of Z-mode. The red and blue lines represent electrostatic waves originating at L = 4.033, Mlat = 0.44° and Mlat = −0.44°, respectively. Circles represent locations where the electrostatic wave mode is converted to Z-mode.

characteristic frequencies of the plasma. This location (L = 4.059) aligns with observations of the mode conversion (4.000 < L < 4.100).

(2) The simulation of wave paths reveals that electrostatic waves are reflected at the resonance frequency f_q, and then can smoothly transition into the Z-mode. The Z-mode's wave normal angle decreases during propagation and it can convert into LO mode (KC) at the window if the propagation direction turns to be parallel (θ = 0°) or anti-parallel (θ = 180°). The simulation results also show that the electrostatic waves serve as the energy source for this process.

The current study successfully provides a direct evidence supporting the linear mode conversion theory as a mechanism for the generation of Kilometric Continuum.

Data Availability Statement

The authors are thankful to the Van Allen Probes scientific instrument teams for making their data available to the public at this website (https://spdf.gsfc.nasa.gov/pub/data/rbsp/). The SYM-*H* and *AE* index data was downloaded from http://wdc.kugi.kyoto-u.ac.jp/wdc/Sec3.html.

Acknowledgments

This work is supported by the National Natural Science Foundation of China grants 42074198, 42230209 and 42374215; the Scientific Research Fund of Hunan Provincial Education Department Grants 21A0212, Post-graduate Scientific Research Innovation Project of Hunan Province CX20240804.

References

Benson, R. F. (1975). Source mechanism for terrestrial kilometric radiation. *Geophys. Res. Lett.*, *2*(2), 52–55. https://doi.org/10.1029/GL002i002p00052

Boardsen, S. A., Green, J. L., and Reinisch, B. W. (2008). Comparison of kilometric continuum latitudinal radiation patterns with linear mode conversion theory. *J. Geophys. Res.: Space Phys.*, *113*(A1), A01219. https://doi.org/10.1029/2007JA012319

Budden, K. G. (1980). The theory of radio windows in the ionosphere and magnetosphere. *J. Atmos. Terr. Phys.*, *42*(3), 287–298. https://doi.org/10.1016/0021-9169(80)90036-7

Deng, Z. K., Xiao, F. L., Zhou, Q. H., Zhang, S., Liu, S., Yang, Q. W., Tang, J. W., Kumamoto, A., Miyoshi, Y., … Nakamura, S. (2022). Direct evidence for auroral kilometric radiation propagation into radiation belts based on Arase spacecraft and van Allen probe B. *Geophys. Res. Lett.*, *49*(19), e2022GL100860. https://doi.org/10.1029/2022GL100860

Engel, J., and Kennel, C. (1985). The effects of density gradients on the convective amplification of upper hybrid waves in the magnetosphere. *Planet. Space Sci.*, *33*(11), 1331–1357. https://doi.org/10.1016/0032-0633(85)90013-3

Fan, K., Gao, X. L., Lu, Q. M., and Wang, S. (2021). Study on electron stochastic motions in the magnetosonic wave field: Test particle simulations. *Earth Planet. Phys.*, *5*(6), 592–600. https://doi.org/10.26464/epp2021052

Gallagher, D. L., Craven, P. D., and Comfort, R. H. (2000). Global core plasma model. *J. Geophys. Res.: Space Phys.*, *105*(A8), 18819–18833. https://doi.org/10.1029/1999JA000241

Green, J. L., Sandel, B. R., Fung, S. F., Gallagher, D. L., and Reinisch, B. W. (2002). On the origin of kilometric continuum. *J. Geophys. Res.: Space Phys.*, *107*(A7), 1105. https://doi.org/10.1029/2001JA000193

Green, J. L., Boardsen, S., Fung, S. F., Matsumoto, H., Hashimoto, K., Anderson, R. R., Sandel, B. R., and Reinisch, B. W. (2004). Association of kilometric continuum radiation with plasmaspheric structures. *J. Geophys. Res.: Space Phys.*, *109*(A3), A03203. https://doi.org/10.1029/2003JA010093

Green, J. L., and Boardsen, S. (2006). Kilometric continuum radiation. *URSI Radio Sci. Bull.*, *2006*(318), 34–42. https://doi.org/10.23919/URSIRSB.2006.7909567

Guan, C. Y., Shang, X. J., Xie, Y. Q., Yang, C., Zhang, S., Liu, S., and Xiao, F. L. (2020). Generation of simultaneous H^+ and He^+ band EMIC waves in the nightside radiation belt. *Sci. China Technol. Sci.*, *63*(11), 2369–2374. https://doi.org/10.1007/s11431-019-1545-6

Guo, M. Y., Zhou, Q. H., Xiao, F. L., Liu, S., He, Y. H., and Yang, C. (2020). Upward propagation of lightning-generated whistler waves into the radiation belts. *Sci. China Technol. Sci.*, *63*(2), 243–248. https://doi.org/10.1007/s11431-018-9486-9

Gurnett, D. A., Kurth, W. S., Roux, A., Bolton, S. J., and Kennel, C. F. (1996). Evidence for a magnetosphere at Ganymede from plasma-wave observations by the Galileo spacecraft. *Nature*, *384*(6609), 535–537. https://doi.org/10.1038/384535a0

Hashimoto, K., Calvert, W., and Matsumoto, H. (1999). Kilometric continuum observed with Geotail. *Adv. Space Res.*, *24*(1), 63–66. https://doi.org/10.1016/S0273-1177(99)00425-1

Hashimoto, K., Anderson, R. R., Green, J. L., and Matsumoto, H. (2005). Source and propagation characteristics of kilometric continuum observed with multiple satellites. *J. Geophys. Res.: Space Phys.*, *110*(A9), A09229. https://doi.org/10.1029/2004JA010729

Hashimoto, K., Green, J., Anderson, R. R., and Matsumoto, H. (2006). Review of kilometric continuum. In J. W. LaBelle, et al. (Eds.), *Geospace Electromagnetic Waves and Radiation* (Vol. 687, pp. 37–54). Berlin, Heidelberg: Springer. https://doi.org/10.1007/3-540-33203-0_2

Horne, R. B. (1989). Path-integrated growth of electrostatic waves: The generation of terrestrial myriametric radiation. *J. Geophys. Res.: Space Phys.*, *94*(A7), 8895–8909. https://doi.org/10.1029/JA094iA07p08895

Jones, D. (1976). Source of terrestrial non-thermal radiation. *Nature*, *260*(5553), 686–689. https://doi.org/10.1038/260686a0

Jones, D. (1981). Beaming of terrestrial miriametric radiation. *Adv. Space Res.*, *1*(1), 373–376. https://doi.org/10.1016/0273-1177(81)90137-X

Kalaee, M. J., and Katoh, Y. (2016). Study of a condition for the mode conversion from purely perpendicular electrostatic waves to electromagnetic waves. *Phys. Plasmas*, *23*(7), 072119. https://doi.org/10.1063/1.4958945

Kletzing, C. A., Kurth, W. S., Acuna, M., MacDowall, R. J., Torbert, R. B., Averkamp, T., Bodet, D., Bounds, S. R., Chutter, M., … Tyler, J. (2013). The electric and magnetic field instrument suite and integrated science (EMFISIS) on RBSP. *Space Sci. Rev.*, *179*(1-4), 127–181. https://doi.org/10.1007/s11214-013-9993-6

Li, P., Zhang, S., Xiao, F. L., Yang, H. M., Ye, S. Y., Liu, S., He, Y. H., Yang, Q. W., Tang, J. W., and Johnston, A. J. (2024). Annual and seasonal occurrence pattern of auroral kilometric radiation associated with the interplanetary magnetic field. *Astrophys. J. Lett.*, *966*(2), L26. https://doi.org/10.3847/2041-8213/ad40a7

Li, T., Liu, S., Yang, C., Xiao, F. L., Yang, H. M., Zhang, S., Gao, Z. L., He, Q., Zhou, Q. H., and He, Y. H. (2023). Direct evidence for efficient scattering of suprathermal electrons by whistler mode waves in the Martian magnetosphere. *Earth Planet. Phys.*, *7*(6), 607–614. https://doi.org/10.26464/epp2023086

Long, M. Y., Gu, X. D., Ni, B. B., Cao, X., Ma, X., and Zhao, Y. W. (2021). Global distribution of electrostatic electron cyclotron harmonic waves in Saturn's magnetosphere: A survey of over-13-year Cassini RPWS observations. *J. Geophys. Res.: Planets*, *126*(4), e2020JE006800. https://doi.org/10.1029/2020JE006800

Menietti, J. D., Santolik, O., Pickett, J. S., and Gurnett, D. A. (2005). High resolution observations of continuum radiation. *Planet. Space Sci.*, *53*(1-3), 283–290. https://doi.org/10.1016/j.pss.2004.09.054

Menietti, J. D., Averkamp, T. F., Ye, S. Y., Sulaiman, A. H., Morooka, M. W., Persoon, A. M., Hospodarsky, G. B., Kurth, W. S., Gurnett, D. A., and Wahlund, J. E. (2018). Analysis of intense *Z*-mode emission observed during the Cassini proximal orbits. *Geophys. Res. Lett.*, *45*(14), 6766–6772. https://doi.org/10.1002/2018GL077354

Morgan, D. D., and Gurnett, D. A. (1991). The source location and beaming of terrestrial continuum radiation. *J. Geophys. Res.: Space Phys.*, *96*(A6), 9595–9613. https://doi.org/10.1029/91JA00314

Spence, H. E., Reeves, G. D., Baker, D. N., Blake, J. B., Bolton, M., Bourdarie, S., Chan, A. A., Claudepierre, S. G., Clemmons, J. H., … Thorne, R. M. (2013). Science goals and overview of the radiation belt storm probes (RBSP) energetic particle, composition, and thermal plasma (ECT) suite on NASA's van Allen probes mission. *Space Sci. Rev.*, *179*(1-4), 311–336. https://doi.org/10.1007/s11214-013-0007-5

Xiao, F. L., Chen, L. J., Zheng, H. N., and Wang, S. (2007). A parametric ray tracing study of superluminous auroral kilometric radiation wave modes. *J. Geophys. Res.: Space Phys.*, *112*(A10), A10214. https://doi.org/10.1029/2006JA012178

Xiao, F. L., Zhou, Q. H., Su, Z. P., He, Z. G., Yang, C., Liu, S., He, Y. H., and Gao, Z. L. (2016). Explaining occurrences of auroral kilometric radiation in Van Allen radiation belts. *Geophys. Res. Lett.*, *43*(23), 11971–11978. https://doi.org/10.1002/2016GL071728

Xiao, F. L., Tang, J. W., Zhang, S., Zhou, Q. H., Liu, S., He, Y. H., Yang, Q. W., Kasahara, Y., Miyoshi, Y., … Nakamura, S. (2022). Asymmetric distributions of auroral kilometric radiation in Earth's northern and southern hemispheres observed by the Arase satellite. *Geophys. Res. Lett.*, *49*(13), e2022GL099571. https://doi.org/10.1029/2022GL099571

Zhang, S., Liu, S., Li, W. T., He, Y. H., Yang, Q. W., Xiao, F. L., Kumamoto, A., Miyoshi, Y., Nakamura, Y., … Shinohara, I. (2021). A concise empirical formula for the field-aligned distribution of auroral kilometeric radiation based on Arase satellite and Van Allen probes. *Geophys. Res. Lett.*, *48*(8), e2021GL092805. https://doi.org/10.1029/2021GL092805

Zhang, S., Yin, Q. P., Yang, H. M., Xiao, F. L., Zhou, Q. H., Yang, Q. W., Tang, J. W., Deng, Z. K., Kasahara, Y., … Hori, T. (2024). Direct observation of L-X mode of auroral kilometric radiation in the lower latitude magnetosphere by the Arase satellite. *Geophys. Res. Lett.*, *51*(5), e2023GL105694. https://doi.org/10.1029/2023gl105694

Zhou, Q. H., Chen, Y. X., Xiao, F. L., Zhang, S., Liu, S., Yang, C., He, Y. H., and Gao, Z. L. (2022). A machine-learning-based electron density (MLED) model in the inner magnetosphere. *Earth Planet. Phys.*, *6*(4), 350–358. https://doi.org/10.26464/epp2022036